The Astrophysical Journal, 880:53 (12pp), 2019 July 20 https://doi.org/10.3847/1538-4357/ab24ca

Probing the Pulsar Population of Terzan 5 via Spectral Modeling

H. Ndiyavala[1,2], C. Venter[1], T. J. Johnson[3], A. K. Harding[4], D. A. Smith[5], P. Eger[6], A. Kopp[1,7], and D. J. van der Walt[1]

[1] Centre for Space Research, North-West University, Potchefstroom Campus, Private Bag X6001, Potchefstroom 2520, South Africa
[2] University of Namibia, Khomasdal Campus, Private Bag 13301, Windhoek, Namibia
[3] College of Science, George Mason University, Fairfax, VA 22030, Resident at Naval Research Laboratory, Washington, DC 20375, USA
[4] Astrophysics Science Division, NASA Goddard Space Flight Center, Greenbelt, MD 20771, USA
[5] Centre d'Études Nucléaires de Bordeaux Gradignan, IN2P3/CNRS, Université Bordeaux 1, BP120, F-33175 Gradignan Cedex, France
[6] Universität Erlangen-Nürnberg, Physikalisches Institut, Erwin-Rommel-Str. 1, D-91058 Erlangen, Germany
[7] Institut für Theoretische Physik IV, Ruhr-Universität Bochum, D-44780 Bochum, Germany
Received 2019 March 15; revised 2019 May 20; accepted 2019 May 23; published 2019 July 24

Abstract

Terzan 5 is the only Galactic globular cluster that has plausibly been detected at very high energies by the High Energy Stereoscopic System. It has an unexpectedly asymmetric very high energy morphology that is offset from the cluster center, in addition to a large-scale, offset radio structure and compact diffuse X-ray emission associated with this cluster. We present new data from the *Fermi* Large Area Telescope on this source. We model the updated broadband spectral energy distribution, attributing this to cumulative pulsed emission from a population of embedded millisecond pulsars, as well as unpulsed emission from the interaction of their leptonic winds with the ambient magnetic and soft-photon fields. In particular, our model invokes unpulsed synchrotron and inverse Compton components to model the radio and TeV data and cumulative pulsed curvature radiation to fit the *Fermi* data, and it explains the hard *Chandra* X-ray spectrum via a "new" cumulative synchrotron component from electron–positron pairs within the pulsar magnetospheres that has not been implemented before. We find reasonable spectral fits for plausible model parameters. We also derive constraints on the millisecond pulsar luminosity function using the diffuse X-ray data and the *Chandra* sensitivity. Future higher-quality spectral and spatial data will help discriminate between competing scenarios (such as dark matter annihilation, white dwarf winds, or hadronic interactions) proposed for the broadband emission, as well as constraining degenerate model parameters.

Key words: globular clusters: individual (Terzan 5) – pulsars: general – radiation mechanisms: non-thermal

1. Introduction

Discovered in the 1960s, the Galactic globular cluster (GC) Terzan 5 is a fascinating object lying at a distance $d = 5.9 \pm 0.5$ kpc (Valenti et al. 2007) and having a particularly high central stellar density, as well as high metallicity. It also has the highest stellar interaction rate of all Galactic GCs (Verbunt & Hut 1987), which is probably linked to the large number of X-ray binaries found in this system. The latter may furthermore explain the fact that Terzan 5 hosts the largest number of millisecond pulsars (MSPs; $N_{\rm vis}^{\rm rad} = 37$ visible in the radio band) of all Galactic GCs (Cadelano et al. 2018), MSPs being the offspring of low-mass X-ray binaries (Camilo & Rasio 2005; Abdo et al. 2010). The discovery of two distinct stellar populations with different iron content and ages in this GC has been interpreted as an indication that Terzan 5 may not be a "true" GC in the usual sense: it may represent the merger of two stellar clusters, or it may be the remnant of a disrupted galaxy (Ferraro et al. 2009). The high metallicity probably points to a very large number of supernova explosions (i.e., progenitors of neutron stars) occurring in Terzan 5, further explaining why this cluster harbors so many MSPs. Moreover, the latter leads to the expectation that even more MSPs may be found in Terzan 5 than the current 37 known ones[8] (Lanzoni et al. 2010; Freire et al. 2017; Cadelano et al. 2018). As such, this GC has been an attractive source to model and observe, since MSPs are known not only to radiate pulsed emission in multiple wavebands but to generate relativistic particles that may in turn upscatter ambient photons into the very high energy (VHE) domain (Bednarek & Sitarek 2007) or interact with the cluster magnetic field to yield diffuse synchrotron radiation (SR; Venter & de Jager 2008).

The *Fermi* Large Area Telescope (LAT; Atwood et al. 2009) has detected a bright GeV source that is very plausibly associated with Terzan 5 (Abdo et al. 2010; Nolan et al. 2012), bringing the total number of LAT sources that are associated with GCs up to about 20 (Acero et al. 2015; Zhang et al. 2016). De Menezes et al. (2018) recently performed a systematic study of 23 *Fermi* GC candidates and detected Terzan 5 at more than 60σ. The High Energy Stereoscopic System (H.E.S.S.) has furthermore detected an extended source in the direction of Terzan 5, although its morphology is peculiar and offset from the GC center (Abramowski et al. 2011b). This makes Terzan 5 the only GC plausibly detected at VHEs (Aharonian et al. 2009; Anderhub et al. 2009; McCutcheon et al. 2009; Abramowski et al. 2011a, 2013). (See Tam et al. 2016 for a recent review of γ-ray detections of GCs.) Diffuse X-rays have also been detected from this GC, peaking at the center and decreasing with cluster radius (Eger et al. 2010). Radio observations have revealed several extended structures in the vicinity of this source (Clapson et al. 2011). In light of the available multiwavelength data and the unique and unexpected source morphology in different energy bands, this source represents a prime subject for deeper investigation.

Several models have attempted to explain the broadband emission properties of GCs. The first class of models invokes

[8] http://www.naic.edu

MSPs as sources of relativistic particles and cumulative high-energy (HE) emission. Chen (1991) provided an early estimate of the cumulative γ-ray luminosity from a population of MSPs embedded in a GC, finding $L_{\gamma,\mathrm{tot}} \sim 10^{36} n_{500}\,\mathrm{erg\,s^{-1}}$ for $n_{500} = N^{\gamma}_{\mathrm{MSP}}/500$ and $N^{\gamma}_{\mathrm{MSP}}$ the number of γ-ray-bright MSPs when convolving the predicted L_{γ} for each pulsar with an expected distribution of periods of GC MSPs (see also Bhatia et al. 1992). This estimate turns out to be correct to within a factor of a few compared to the measured GeV luminosities for some *Fermi*-detected GCs (e.g., Abdo et al. 2010) if one sets $n_{500} \sim 0.2$. Wei et al. (1996) calculated such a cumulative γ-ray flux using an outer gap model. Comparing their expected flux level for unpulsed γ-rays to an upper limit by the EGRET, they constrained $n_{500} < 0.8$ for 47 Tucanae. Harding et al. (2005), Venter & de Jager (2008), and Venter et al. (2009) summed the individual pulsed curvature radiation (CR) spectra from their model for an ensemble of MSPs to estimate the GeV flux expected from a GC, and the predictions of Venter et al. (2009) provided a good match to the subsequent *Fermi* measurements of the HE spectrum of 47 Tucanae (Abdo et al. 2009). Cheng et al. (2011) investigated an alternative scenario to produce GeV emission by attributing this to inverse Compton (IC) rather than CR emission, also predicting GCs to be extended sources in the GeV regime. Conversely, Bednarek & Sitarek (2007) predicted that GCs may be pointlike sources of GeV and TeV emission by considering MSPs that accelerate leptons either at the shocks that originate during collisions of the respective pulsar winds or inside the pulsar magnetospheres. The leptons escape from these local acceleration sites, diffuse outward, and interact with the GC magnetic and soft-photon background fields. This leads to SR and IC scattering (see Venter et al. 2009 and Zajczyk et al. 2013 for updated calculations). Kopp et al. (2013) presented an improved model and found reasonable fits to the multiband spectral energy distribution (SED) data of Terzan 5. Ndiyavala et al. (2018) applied this model to the Galactic population of GCs, ranking them according to predicted VHE flux.

There exist alternative models that invoke other astrophysical objects as sources of relativistic particles. Bednarek (2012) calculated the contribution of nonaccreting white dwarfs in GCs to the γ-ray flux from such clusters and concluded that white dwarfs may produce γ-ray emission at a level that may be detectable by the Cerenkov Telescope Array (CTA) in some cases. See Bednarek (2011) for a review of the leptonic GC models. On the other hand, Domainko (2011) investigated a hadronic model, invoking a γ-ray burst remnant as a potential source of energetic leptons and hadrons. In this model, the hadrons interact with ambient target nuclei, leading to the formation of π^0 particles that decay into γ-rays. Recently, Brown et al. (2018) concluded[9] that a combination of MSP pulsed curvature emission and dark matter annihilation (with an enhanced density around a putative intermediate-mass black hole) may explain the GeV emission detected by *Fermi* LAT for 47 Tucanae.

[9] These authors themselves noted that their work does not rule out an MSP-only explanation for the GeV flux seen from 47 Tucanae. They used the average spectrum of *Fermi*-detected MSPs, assuming this to be universal and allowing only the spectral normalization to be free. Other effects, such as the inclusion of MSPs that are below detection threshold, as well as different MSP geometries (inclination and viewing angles), may change the low-energy spectral shape, hardening it to potentially bring it into better agreement with the data without the need to invoke dark matter annihilation (the latter model has several more free parameters, and a combination of MSPs and dark matter may therefore naturally better account for the data).

Even though models are making progress to explain the broadband emission of GCs, many questions remain. For example, Venter & Kopp (2015b) noted that uncertainties in the model parameters may lead to a spread in the predicted GC flux of up to an order of magnitude. They attempted to mitigate this problem by considering an ensemble of observed GCs to constrain their models, using a H.E.S.S. upper limit (Abramowski et al. 2013) to the cumulative flux from 15 GCs (Venter & Kopp 2015a, 2015b; H. Ndiyavala et al. 2019, in preparation), but some parameter degeneracies are expected to remain. The hard slope of the diffuse X-ray emission in the case of Terzan 5 poses another puzzle, since the existing models have not been able to fit this component (e.g., Kopp et al. 2013). The energy-dependent morphology (which is nonspherical at high energies) further challenges the existing models. Bednarek & Sobczak (2014) considered a model where energetic particles escape from the GC and interact with the Galactic medium, creating a bow shock nebula around the GC. If the latter is immersed in the relatively dense medium close to the Galactic plane, this should manifest as an intricate morphology at high energies. To further address this complex morphology, Bednarek et al. (2016) extended their model to take into account the advection of leptons by a mixture of red giant stellar and pulsar winds, as well as considering the effect of having a noncentral (offset) energetic MSP as a source of relativistic particles. Furthermore, in the case of Terzan 5, the source morphologies differ significantly in extent and position across the electromagnetic spectrum, raising the question of whether all of the spectral components arise due to the same underlying particle population (in the leptonic scenario). Lastly, the operation of different emission mechanisms and relative contribution of MSPs versus other astrophysical sources or dark matter to the SED remains an open question.

Given the richness of the existing data set on Terzan 5, as well as the variety of models that exist to explain GC emission (and their many free parameters), we use this system as a case study to further probe the origin of multiwavelength emission from GCs. Improved models will aid the selection of promising GCs for future observations by the CTA, which may see tens of these sources in the next decade (Ndiyavala et al. 2018). We therefore aimed to gather more data on Terzan 5 (Section 2) and model the updated SED in a leptonic scenario (Section 3.2). We present our conclusions in Section 4.

2. Multiwavelength Data and Spectral Upper Limits

2.1. Previous Radio Observations

Individual MSP discoveries in Terzan 5 bring the total membership to 37 (e.g., Lyne et al. 1990, 2000; Ransom et al. 2005; Hessels et al. 2006; Freire et al. 2017; Cadelano et al. 2018),[10] although hundreds of MSPs may be present following expectations of numerical simulations (Ivanova et al. 2008). Fruchter & Goss (2000) obtained images of Terzan 5 at 6, 20, and 90 cm using the Very Large Array (VLA). These displayed strong, steep-spectrum emission that could not be associated with known pulsars at that time. Numerous point sources were also detected within 30″ of the cluster center, with their density rising rapidly toward the core. There, an elongated region of emission was found. Based on the steep spectrum, as well as the flux distribution, Fruchter & Goss (2000) concluded that

[10] http://www.naic.edu/~pfreire/GCpsr.html

this probably indicated the presence of many undetected pulsars in the cluster, making this the most pulsar-rich of all Galactic GCs (they estimated a total number of 60–200 host pulsars, based on their assumed radio luminosity function).

Terzan 5 was furthermore detected in the NRAO VLA Sky Survey (NVSS) at 21 cm as a single source with a flux of about 5 mJy (Condon et al. 1998). Clapson et al. (2011) analyzed archival 11 and 21 cm Effelsberg data and detected several radio structures in the direction of Terzan 5. However, given the uncertainty in flux, no spectral index could be inferred. Clapson et al. (2011) speculated that one structure[11] in particular (labeled as "Region 11"), extending from the GC center to the northwest (roughly perpendicular to the Galactic plane), could be the result of SR by electrons escaping from the large population of MSPs in this GC. In what follows, we fit these radio data using a diffuse low-energy SR (LESR) component due to the interaction of relativistic electrons escaping from the MSP magnetospheres with the cluster B-field (see Figure 1). The contribution of the population of unresolved MSPs to this diffuse radio flux is negligible and can be ignored.[12]

2.2. Optical Upper Limits: Comparison of Thermal and Nonthermal Flux Levels

Our predicted nonthermal unpulsed LESR spectral component invoked to model the radio data (Section 3) extends into the optical band, raising the question of its detectability. The LESR component's flux is relatively low in the optical band (Kopp et al. 2013), and we now show that it may, in principle, be very difficult to directly observe it, since there are $\sim 10^5$ stars (point sources) that contribute a high level of blackbody (BB) radiation that will swamp any diffuse nonthermal SR.

To appraise the BB νF_ν flux from stars in different annuli centered on the cluster, as well as the total flux expected from the full cluster, we use the surface-density profile of Terzan 5 obtained by Trager et al. (1995), as converted by Cohn et al. (2002). We estimate the area of an annulus as $A_{\rm ann} = \pi(\theta_2^2 - \theta_1^2)$, where θ_1 and θ_2 are the edges (angular radii) of a particular annulus. The average number of stars in such an annulus is found by interpolating the surface brightness f and calculating $N_{\rm ann} = fA_{\rm ann}$. We approximate the emitted spectrum

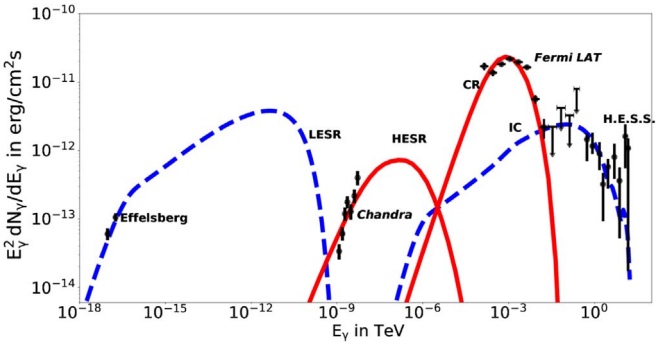

Figure 1. Different spectral components for Terzan 5 predicted by the leptonic models of Kopp et al. (2013) and Harding et al. (2008) and Harding & Kalapotharakos (2015). Using the first model, we calculate the LESR and VHE IC components (integrated over all r_s; dashed blue lines). We assumed $E_{\rm e,min} = 9 \times 10^{-3}$ TeV, $E_{\rm e,max} = 10$ TeV, $Q_0 = 1.4 \times 10^{34}$ erg^{-1} s^{-1}, $B = 4.0\,\mu$G, $\Gamma = 1.5$, and $\kappa = 7 \times 10^{-5}$ kpc^2 Myr$^{-1} \approx 2 \times 10^{25}$ cm^2 s^{-1}. We used a distance of $d = 5.9$ kpc, core radius $R_{\rm c} = 0.15' = 0.26$ pc, half-mass radius $R_{\rm hm} = 0.52' = 0.89$ pc, and tidal radius $R_{\rm t} = 4.6' = 7.9$ pc. The HESR and CR components (red lines) are predictions using the model of Harding et al. (2008) and Harding & Kalapotharakos (2015) for $\langle\alpha\rangle = 45°$, $\langle\zeta\rangle = 60°$, $\langle P\rangle = 7.7 \times 10^{-3}$ s, and $\langle B_{\rm s}\rangle = 5.8 \times 10^9$ G. We also indicate *Chandra* (Eger et al. 2010), H.E.S.S. (Abramowski et al. 2011b), and radio data ("Region 11," as defined by Clapson et al. 2011). The uncertainties in our LAT points do not reflect possible systematic errors on the Galactic diffuse emission model.

of each star by a BB spectrum at a single average frequency $\langle\nu\rangle = 2.7 k_{\rm B} T/h = 2.5 \times 10^{14}$ Hz, where $k_{\rm B}$ is the Boltzmann constant and h is the Planck constant, assuming a constant stellar surface temperature of $T = 4500$ K. Upon multiplying the Planck spectrum B_ν by the stellar surface area $A_\star = 4\pi R_*^2$, with R_* the average stellar radius, and dividing by the square of the distance to the cluster, we obtain the thermal νF_ν flux level,

$$\frac{B_\nu \langle\nu\rangle A_\star}{d^2} = \frac{8\pi R_*^2 h \langle\nu\rangle^4 N_{\rm ann}}{d^2 c^2} \frac{1}{e^{h\nu/k_{\rm B}T} - 1} \sim 1.7 \times 10^{-14} R_{*,10}^2 N_{\rm ann}\ {\rm erg\ cm^{-2}\ s^{-1}}, \quad (1)$$

where $R_{*,10} = R_*/10^{10}$ cm, c is the speed of light, and assuming $d = 5.9$ kpc. When applying Equation (1) to the whole cluster (i.e., choosing $N_* = N_{\rm ann} = 7.7 \times 10^4$; Lang 1992), we find that the predicted BB flux is $\sim 6.2 \times 10^{-8}$ erg cm^{-2} s^{-1} for $R_{10} = 7$, while the predicted νF_ν flux for the LESR at 1 eV is only $\sim 5.0 \times 10^{-12}$ erg cm^{-2} s^{-1} (Section 3), which is a factor of $\sim 10^4$ lower than the estimated thermal flux level. The only hope to detect the LESR component is if the stellar flux falls faster with radius than the LESR flux. One might thus try to obtain a smaller ratio between thermal and nonthermal fluxes by focusing on different annuli. We calculated the flux ratio for all annuli in Cohn et al. (2002) and found that they drop from $\sim 10^5$ to $\sim 10^3$ with increasing radius out to $\sim 0.35 R_{\rm t}$, with $R_{\rm t}$ the tidal radius. Since the annular area increases as r^2 while the surface brightness falls as $r^{-2.1}$ for larger radii, the estimated BB flux remains nearly constant for the outer annuli (with $N_{\rm ann} \sim 10^3$) out to $R_{\rm t}$. Thus, even in the outer annuli, where the stellar density has dropped significantly, the BB flux still exceeds the LESR flux by a factor of 10^3. In some sense, the thermal emission thus provides a very unconstraining upper limit to the LESR emission under the assumption that the latter will not exceed the thermal flux. However, since the BB spectrum covers a much narrower energy

[11] Care should be taken to simply compare the results of Condon et al. (1998) with those of Clapson et al. (2011). The NVSS was done with the VLA in the DnC configuration, and the largest angular scale that can be detected in this most compact configuration is 970″ in full synthesis mode. In snapshot mode, this is 485″. We expect that only the brightest part of the emission would have been detected and that the angular size of the detected region was actually less than 485″. In fact, Condon et al. (1998) gave the size of the emission region as less than 58″ × 47″. Conversely, Clapson et al. (2011) used the Effelsberg single-dish telescope, for which there is no limit to the largest detectable angular size of an extended structure. In the present context, the largest angular scale is of importance. Clapson et al. (2011) listed a size for Region 11 of 720″ × 1080″, even larger than the tidal radius of Terzan 5 of $R_{\rm t} \sim 280''$ and also exceeding the largest angular size detectable at 21 cm with the VLA in the DnC configuration. It thus makes sense that the implied flux measured by Clapson et al. (2011) for Region 11 at 21 cm is ∼4 Jy versus the relatively low flux of ∼5 mJy measured by Condon et al. (1998). However, the surface brightnesses of both observations are quite similar in magnitude. It is unquestionable that the Condon et al. (1998) observations suffered from the "missing-flux effect" of interferometric observations. We conclude that the Clapson et al. (2011) value of the total flux from Region 11 is the more reliable value that should be used in the model fitting.

[12] Ransom et al. (2005) estimated the total flux at 1.95 GHz of 22 MSPs in the core of Terzan 5 to be ∼1 mJy (the scale is $R_{\rm c} \sim 9''$), or up to a few mJy if one adds two more MSPs farther from the GC center, while the flux from the large Region 11 measured by Clapson et al. (2011) of ∼4 Jy dwarfs this value.

range than the LESR, there may yet be hope for detecting the LESR flux outside of the optical range (e.g., the millimeter or ultraviolet to low-X-ray range) where the BB component dominates.

2.3. Diffuse X-Ray Emission

To investigate the X-ray point-source population of Terzan 5, the core of this GC was covered in a deep *Chandra* observation with a field of view of $\sim 5' \times 5'$ (Heinke et al. 2006). Later, by following up on the detection of extended TeV γ-ray emission from the direction of Terzan 5 by H.E.S.S. (Abramowski et al. 2011b), Eger et al. (2010) discovered the presence of hard and diffuse X-ray emission using the same *Chandra* data. The diffuse X-ray signal was shown to be extended well beyond the half-mass radius ($R_{\rm hm} \sim 30''$) of the GC up to $\sim 180''$, featuring a very hard spectrum that may be fit by a power law with a photon index of 0.9 ± 0.5 (see Figure 1). The contribution from unresolved pointlike sources to this diffuse signal was estimated to be very small. They found that the surface brightness peaked near the cluster center and decreased smoothly outward. Various nonthermal emission mechanisms for the origin of this diffuse signal were discussed, but with no single scenario being clearly preferred. A follow-up search for an X-ray signal on similar spatial scales from a number of other LAT-detected GCs covered by archival X-ray observations yielded no additional significant detections (see Eger & Domainko 2012). However, a new hard, diffuse X-ray signal was recently discovered from 47 Tucanae, but on comparatively smaller spatial scales (Wu et al. 2014). In contrast to Terzan 5, the X-ray signal here appears to be contained within the half-mass radius of the GC. The spectrum can be described as a combination of a hard power-law component with a photon index of ~ 1.0 and a thermal plasma component with a temperature of $k_{\rm B}T = 0.2$ keV. The nonthermal X-ray emission detected from both Terzan 5 and 47 Tucanae could be unpulsed SR from relativistic leptons that were accelerated in shocks, following the collision of stellar winds in the GC cores (i.e., a single spectral component explaining both the radio and X-ray data in the case of Terzan 5, although the diffuse X-ray emission appears on very different spatial scales in these two GCs; Bednarek & Sitarek 2007; Venter et al. 2009). However, we cannot find a satisfactory fit to the spectral data of these clusters when invoking only a single SR spectral component. We therefore model the diffuse X-ray emission observed from Terzan 5 by invoking a new component that is due to the cumulative pulsed SR by pairs originating in the various host MSP magnetospheres (Section 3).

2.4. New Fermi LAT Data Analysis

Terzan 5 was the second GC to be associated with a *Fermi* LAT source (Abdo et al. 2010; Kong et al. 2010; Nolan et al. 2012). Comparing the likelihood when modeling the spectrum with a simple power-law shape,

$$\frac{dN}{dE} = N_0 \left(\frac{E}{E_0}\right)^{-\Gamma}, \tag{2}$$

and an exponentially cut off power-law shape,

$$\frac{dN}{dE} = N_0 \left(\frac{E}{E_0}\right)^{-\Gamma} \exp\left\{-\left(\frac{E}{E_{\rm C}}\right)^{b}\right\}, \tag{3}$$

the γ-ray point source associated with Terzan 5 was found to be significantly curved, consistent with the interpretation of the collective emission from a population of MSPs. In both Equations (2) and (3), N_0 is a normalization factor with units $\rm cm^{-2}\,s^{-1}\,MeV^{-1}$, E_0 is a scale parameter, and Γ is the photon index. In Equation (3), $E_{\rm C}$ is the cutoff energy and b is an exponential index that governs how quickly the spectrum rolls over. Low-altitude pulsar emission models predict a super-exponential cutoff with $b > 1$ (e.g., Harding et al. 1978). For some of the brightest γ-ray pulsars, LAT observations require a subexponential cutoff with $b < 1$, plausibly explained as a blending of several simple exponentially cut off spectra as the line of sight crosses different regions of the magnetosphere (Abdo et al. 2013).

Kong et al. (2010) analyzed approximately 1.4 yr of Pass 6 (P6) LAT data from the region around Terzan 5 with energies ranging from 0.5 to 20 GeV and found a significant point source ($18'$) from the optical center of Terzan 5, with a pulsar-like spectrum having a photon index $\Gamma = 1.9 \pm 0.2$, a cutoff energy $E_{\rm C} = 3.8 \pm 1.2$ GeV, and integrated photon and energy fluxes over their energy range of $(3.4 \pm 1.1) \times 10^{-8}$ and $(6.8 \pm 2.0) \times 10^{-11}\,\rm erg\,cm^{-2}\,s^{-1}$, respectively.

Abdo et al. (2010) analyzed the region around Terzan 5 using approximately 1.5 yr of P6 LAT data with energies $\geqslant 0.2$ GeV, including the same time span of Kong et al. (2010). These authors also found a significant point source, located $2\farcm4$ from the cluster center, with a pulsar-like spectrum. Their best-fit simple exponentially cut off power-law spectrum had $\Gamma = 1.4^{+0.2,+0.4}_{-0.2,-0.3}$, $E_{\rm C} = 2.6^{+0.7,+1.2}_{-0.5,-0.7}$ GeV, and integrated photon and energy fluxes over their energy range of $(7.6^{+1.7,+3.4}_{-1.5,-2.2}) \times 10^{-8}$ and $(7.1^{+0.6,+1.0}_{-0.5,-0.5}) \times 10^{-11}\,\rm erg\,cm^{-2}\,s^{-1}$, respectively. The first uncertainties are statistical, while the second reflect estimates of systematic errors. Using an estimate of the average MSP spin-down power and γ-ray efficiency with the measured γ-ray flux, Abdo et al. (2010) estimated the number of MSPs in Terzan 5 to be $N^{\gamma}_{\rm MSP} = 180^{+100}_{-90}$.

Using 4 yr of data, the third *Fermi* LAT catalog (3FGL; Acero et al. 2015) associates 3FGL J1748.0−2447 with Terzan 5. The source is offset from the cluster center[13] by $0\farcm66$, well within the 95% confidence level ellipse with semimajor and semiminor axes of $1\farcm69$ and $1\farcm53$, respectively. The pivot energy for 3FGL J1748.0−2447, 1280.38 MeV, is used as the scale parameter E_0 in our subsequent analyses.

We selected 7 yr of Pass 8 (P8) LAT data[14] (Atwood et al. 2013) from the start of science operations on 2008 August 4, with *evclass* = 128 and *evtype* = 3, within 15° of the best-fit position of 3FGL J1748.0−2447, with energies from 0.1 to 300 GeV, and with a maximum zenith angle of 90°. The *Fermi* ScienceTool[15] (ST) `gtmktime` was used to select good time intervals when the spacecraft was in nominal science operations mode and the data were flagged as good. In preparation for a binned maximum-likelihood analysis, we made a live-time cube using the ST `gtltcube` with *zmax* = 90° and an

[13] The optical and diffuse X-ray centers are more or less coincident. The center of the radio Region 11 is offset from this position by $\sim 14'$, while that of the extended H.E.S.S. source is offset by $\sim 4'$ (compared to a tidal radius of $R_{\rm t} = 4\farcm6$).

[14] http://fermi.gsfc.nasa.gov/ssc/data/analysis/documentation/Pass8_usage.html

[15] Available for download at https://fermi.gsfc.nasa.

exposure cube with 35 bins in $\log_{10}$ energy and spatial pixels 0.°1 on a side using the ST `gtexpcube2` and the P8R2_SOURCE_V6 LAT Instrument Response Functions.

We constructed a model of our region of interest (ROI) including all 3FGL sources within 25° of the ROI center; those sources known to be extended were modeled using the spatial templates from the catalog. The spectral parameters of sources >6° from the ROI center were held fixed at the values from 3FGL. For sources within 6° of the ROI center, the spectral parameters were allowed to vary if they were found to have an average significance $\geqslant 15\sigma$ in 3FGL. However, for sources within 8° of the ROI center that did not otherwise satisfy our requirements for free spectral parameters but were flagged as significantly variable in 3FGL, we did allow the normalization parameters to vary. The diffuse emission from the Milky Way was included using the *gll_iem_v06.fits* model, while the isotropic diffuse emission and residual background of misclassified cosmic rays were modeled using the *iso_P8R2_SOURCE_V6_v06.txt* template (Acero et al. 2016). We allowed the intensity of the Galactic diffuse emission to be modified by a power-law spectrum.

The spectrum of 3FGL J1748.0−2447 was found to have significant curvature and thus modeled using a log-parabola function in the catalog. For our purposes, we modeled the spectrum of 3FGL J1748.0−2447 using both a simple power law (Equation (2)) and an exponentially cut off power law (Equation (3)). We performed three binned maximum-likelihood analyses, with energy dispersion disabled, with the spectrum of 3FGL J1748.0−2447 modeled as a power law, a simple exponentially cut off power law, and an exponentially cut off power law with the b parameter allowed to vary. Following Abdo et al. (2013), we compared the best-fit likelihood value from the fit using a power law ($\mathcal{L}_{\rm pl}$) to that when using a simple cutoff ($\mathcal{L}_{\rm co}$ when $b = 1$) to calculate a Test Statistic $\mathrm{TS_{cut}} = -2(\ln(\mathcal{L}_{\rm co}) - \ln(\mathcal{L}_{\rm pl})) = 207$, significantly favoring the cutoff model over the power law. Similarly, we found $\mathrm{TS_{bfree}} = -2(\ln(\mathcal{L}_{\rm bfree}) - \ln(\mathcal{L}_{\rm co})) = 4$, where $\mathcal{L}_{\rm bfree}$ is the best-fit likelihood when modeling the spectrum of 3FGL J1748.0−2447 as an exponentially cut off power law with the b parameter free. As such, there is no preference for the fit with b free, and we use the results from the simple exponentially cut off power law, which are reported in Table 1. In addition to the fit parameters from Equation (3), Table 1 also includes the integrated photon (F) and energy (G) fluxes from 0.1 to 300 GeV derived from the best-fit models. Our best-fit energy flux agrees well with that of de Menezes et al. (2018), who reported a value of $G_{100} = (7.44 \pm 0.27) \times 10^{-11}$ erg cm^{-2} s^{-1} (rounded so that there are two significant figures in the error), over the energy range 0.1–100 GeV, using 9 yr of P8 data, and assuming a log-parabola spectral shape. A residual TS map of the region around 3FGL J1748.0−2447, using our best-fit $b = 1$ model, did not reveal the need for adding any new sources to our model, even though the data sets we analyzed covered 3 more yr than that used for the 3FGL catalog.

While our likelihood analyses did successfully converge, the fits of the entire region were formally bad. In particular, there were large residuals starting at ∼10 GeV, growing to larger discrepancies out to 300 GeV. The preliminary 8 yr LAT source catalog[16] with an improved Galactic diffuse model and P8R3 data and using weighted likelihood (*Fermi* LAT Collaboration 2019) finds much better residuals in the region around Terzan 5. This catalog used a different functional form for the spectrum of the source associated with Terzan 5 (4FGL J1748.0−2446) and fixed $b = 2/3$, but we can still compare the flux values. The source 4FGL J1748.0−2446 has a reported integral photon flux above 1 GeV of $(1.26 \pm 0.03) \times 10^{-8}$ cm^{-2} s^{-1}, which is larger than the value of $(1.05 \pm 0.03) \times 10^{-8}$ cm^{-2} s^{-1} found in our analysis. Our best-fit Γ value agrees with both previous studies (Abdo et al. 2010; Kong et al. 2010) within their quoted uncertainties. The best-fit $E_{\rm C}$ of Kong et al. (2010) agrees with our value within the uncertainty, but that of Abdo et al. (2010) is significantly lower. Using our P8 results, we find photon and energy fluxes over the 0.5–20 GeV energy range of $(2.3 \pm 0.1) \times 10^{-8}$ and $(5.3 \pm 0.1) \times 10^{-11}$ erg cm^{-2} s^{-1}. While both values are lower than those reported by Kong et al. (2010), they agree within the uncertainties. Integrating above 0.2 GeV, our model yields photon and energy fluxes of $(5.4 \pm 0.2) \times 10^{-8}$ and $(6.8 \pm 0.2) \times 10^{-11}$ erg cm^{-2} s^{-1}. These values are also lower than those reported by Abdo et al. (2010) but agree within the uncertainties, and we note that the energy flux values (often more reliable, as noted by Abdo et al. 2013) agree well.

Table 1
LAT Spectral Fit Results

N_0 (10^{-11} cm^{-2} s^{-1} MeV^{-1})	1.04 ± 0.40
Γ	1.71 ± 0.04
$E_{\rm C}$ (GeV)	4.61 ± 0.35
F_{100} (10^{-8} cm^{-2} s^{-1})	9.68 ± 0.52
G_{100} (10^{-11} erg cm^{-2} s^{-1})	7.79 ± 0.22
$\mathrm{TS_{cut}}$	207
$\mathrm{TS_{bfree}}$	4

We produced spectral points by dividing the 0.1–300 GeV interval into 12 bins, equally sized in $\log_{10}$ energy, and performing binned likelihood fits assuming a power-law form for the spectrum of 3FGL J1748−2447 with $\Gamma = 2$ and only the normalization parameters of other sources left free. We report a flux value, with uncertainty, for those bins where 3FGL J1748−2447 was detected with a point-source $\mathrm{TS} \geqslant 9$ ($\sim 3\sigma$) and at least 4 predicted counts, otherwise a 95% confidence level flux upper limit is reported. The flux upper limits were calculated using the Bayesian method for energy bins with point-source $\mathrm{TS} \leqslant 0$ or <4 predicted counts from 3FGL J1748−2447. For plotting and to produce the E^2dN/dE points, we used the logarithmic mean of each energy bin (see Figure 1). In Section 3, we model the *Fermi* LAT spectrum as originating due to the cumulative pulsed CR by the embedded MSPs.

In order to search for γ-ray pulsations, we obtained timing solutions for 33 of the pulsars in Terzan 5 (namely, PSRs J1748−2446aa, ab, ac, ae, af, ag, ah, ai, aj, ak, C, D, E, F, G, H, I, J, K, L, M, N, O, Q, R, S, T, U, V, W, X, Y, and Z) that were valid from before the launch of *Fermi* until 2012 July (S. Ransom 2019, personal communication[17]). We used the ephemerides for pulsars aj and ak from Cadelano et al. (2018). Using the best-fit maximum-likelihood model, in which the spectrum of 3FGL J1748.0−2447 was modeled as a simple exponentially cut off power law, we calculated spectral weights for events within 2° of the best-fit position. For each event, the weight reflects the probability that the event originated from

[16] Available at https://fermi.gsfc.nasa.gov/ssc/data/access/lat/8yr_catalog/.

[17] https://www.cv.nrao.edu/~sransom/Ter5_index.html

3FGL J1748.0−2447. Use of these weights has been shown to enhance the sensitivity of γ-ray pulsation searches (Kerr 2011). We then used the timing solutions mentioned above to search for modulations in γ-ray events at the spin and orbital periods from known pulsars in Terzan 5. We tested for modulation at the spin period using the H test (de Jager et al. 1989; de Jager & Büsching 2010), modified to include spectral weights (Kerr 2011). For those pulsars in binary systems, we used both the H test and the Z_m^2 test with $m = 2$ harmonics when testing for modulation at the orbital period. When performing the search for orbital modulation, we corrected for exposure variations as described in Johnson et al. (2015). We tested for spin pulsations using both the full data set and only events up to the end of each ephemeris's validity interval. No significant modulation was detected from any pulsar for which we had a timing solution, with a maximum signal of 2.2σ.

2.5. H.E.S.S. Data

H.E.S.S. discovered a VHE γ-ray source in the direction of Terzan 5 (Abramowski et al. 2011b). The integral flux above 440 GeV of the source was measured as $(1.2 \pm 0.3) \times 10^{-12}\,\mathrm{cm^{-2}\,s^{-1}}$, and its spectrum was best described by a single power law with an index of $2.5 \pm 0.3_{\mathrm{stat}} \pm 0.2_{\mathrm{sys}}$. The VHE source is offset from the center of the GC by $4\farcm0 \pm 1\farcm9$ (about 7 pc at a distance of 5.9 kpc), with its size being characterized by widths from a 2D Gaussian fit of $9\farcm6 \pm 2\farcm4$ and $1\farcm8 \pm 1\farcm2$ for the major and minor axes (compared to the GC tidal radius of $R_{\mathrm{t}} = 4\farcm6$). The source is oriented $92° \pm 6°$ westward from north.[18] A chance coincidence between Terzan 5 and an unrelated VHE γ-ray source is rather unlikely ($\sim 10^{-4}$). Ndiyavala et al. (2018) reanalyzed Terzan 5 data and obtained a significance of 6σ for standard and loose cuts and 7.1σ for hard cuts that compare well with that of Abramowski et al. (2011b), who obtained a significance of 5.3σ.

3. Modeling the Broadband SED

3.1. Parameter Constraints from General Considerations

In this section, we derive general constraints on the spatial diffusion coefficient κ (for simplicity, we assume that this coefficient is only a function of particle energy, not of space) and the cluster B-field.

As a first approach, the Bohm value has been used in the past to model the particle diffusion (Bednarek & Sitarek 2007; Venter & de Jager 2008),

$$\kappa_{\mathrm{Bohm}} = \frac{cE_{\mathrm{e}}}{3eB} = 3.3 \times 10^{25} E_{\mathrm{TeV}} B_{-6}^{-1}\ \mathrm{cm^2\,s^{-1}}, \tag{4}$$

with $E_{\mathrm{TeV}} = E_{\mathrm{e}}/1$ TeV the particle energy and $B_{-6} = B/1\ \mu$G. By invoking a containment argument, one may obtain a constraint on this coefficient: since we observe VHE γ-ray emission up to $E_\gamma \sim 10$ TeV, one can write that the diffusion time (in the limit that it exceeds the escape time) should exceed the typical timescale for IC emission:

$$\tau_{\mathrm{esc}} > \tau_{\mathrm{IC}}. \tag{5}$$

[18] This means that the H.E.S.S. source is much closer to the GC core than the radio Region 11, and it only slightly overlaps with its inner edge.

This leads to

$$\frac{R^2}{6\langle\kappa\rangle} > \frac{E_{\mathrm{e}}}{\dot{E}_{\mathrm{IC}}}. \tag{6}$$

Let us concentrate on the optical soft-photon background with photons at $T \sim 4500$ K (i.e., having an average energy $\langle\epsilon\rangle \sim 1$ eV). For very energetic leptons, we have to take Klein–Nishina effects into account when calculating the IC loss rate. We thus use the expression of Schlickeiser & Ruppel (2010),

$$\dot{E}_{\mathrm{IC}} \approx \frac{4\sigma_{\mathrm{T}} cu}{3} \frac{\gamma_{\mathrm{e}}^2 \gamma_{\mathrm{KN}}^2}{\gamma_{\mathrm{e}}^2 + \gamma_{\mathrm{KN}}^2}, \tag{7}$$

with $\sigma_{\mathrm{T}} = 6.65 \times 10^{-25}\,\mathrm{cm^2}$ the Thomson cross section, u the average soft-photon energy density, and

$$\gamma_{\mathrm{KN}} \equiv \frac{3\sqrt{5}}{8\pi} \frac{m_{\mathrm{e}} c^2}{k_{\mathrm{B}} T} \tag{8}$$

the critical Klein–Nishina Lorentz factor. If the particle Lorentz factor $\gamma_{\mathrm{e}}^2 \gg \gamma_{\mathrm{KN}}^2$, the IC loss rate reduces to

$$\dot{E}_{\mathrm{IC}} \approx \frac{4\sigma_{\mathrm{T}} cu\gamma_{\mathrm{KN}}^2}{3}, \tag{9}$$

yielding

$$\begin{aligned} \tau_{\mathrm{IC}} &\approx 6 \times 10^{12} \left(\frac{E_{\mathrm{TeV}} T_{4500}^2}{u_{50}} \right)\ \mathrm{s} \\ &\approx 2 \times 10^{5} \left(\frac{E_{\mathrm{TeV}} T_{4500}^2}{u_{50}} \right)\ \mathrm{yr}, \end{aligned} \tag{10}$$

with $u_{50} \equiv u/(50\ \mathrm{eV\,cm^{-3}})$ and $T_{4500} = T/4500$ K. We use u_{50} to scale our results, since this value reflects a spatially averaged value for the energy density; see Figure 1 of Bednarek & Sitarek (2007) and Prinsloo et al. (2013). If we set $R \sim R_{\mathrm{t}} \sim 10$ pc, we find

$$\langle\kappa\rangle < 2.6 \times 10^{25} \left(\frac{R_{10}^2 u_{50}}{E_{\mathrm{TeV}} T_{4500}^2} \right)\ \mathrm{cm^2\,s^{-1}}, \tag{11}$$

with $R_{10} \equiv R/10$ pc and R_{t} the tidal radius. This upper limit is similar to the value of the Bohm coefficient at $E_{\mathrm{e}} = 1$ TeV. Kopp et al. (2013) inferred values for κ that are slightly larger at 1 TeV than the Bohm value (for $B_{-6} \sim 5$) when fitting the X-ray surface brightness profile, although they assumed an energy dependence $\kappa \propto E_{\mathrm{e}}^{0.6}$. They also noted that by assuming Bohm diffusion, they could fit the X-ray surface brightness data, and that the degeneracy in diffusion index and normalization may be broken by using spatial data in a different waveband, as well as more spectral data. The caveat is that both the spatial and spectral fit should be reasonable. While Kopp et al. (2013) could fit the X-ray surface brightness profile, their predicted SED did not match the data. We thus update their calculation so as to fit both these quantities (Section 3.2).

Additionally, one may argue that since we observe IC emission up to $E_\gamma \sim 10$ TeV, we must have

$$\tau_{\mathrm{SR}} \gtrsim \tau_{\mathrm{IC}}. \tag{12}$$

This implies (at those high energies) that

$$\dot{E}_{\rm SR} \lesssim \dot{E}_{\rm IC}, \tag{13}$$

which yields a limit on the magnetic field

$$B_{-6} \lesssim 8\left(\frac{\sqrt{u_{50}}}{T_{4500}E_{\rm TeV}}\right). \tag{14}$$

Therefore, from the simple arguments above, we find typical values of $B_{-6} \sim 10$ and $\langle\kappa\rangle \sim 5 \times 10^{25}$ cm^2 s^{-1} around $E_{\rm TeV} \sim 1$, similar to what was found by Kopp et al. (2013). At these typical cluster B-fields, the LESR spectrum should peak around

$$E_\gamma = 0.29h\nu_{\rm crit} \approx 2 \times 10^{-5}B_{-6}E_{\rm TeV}^2 \ \ {\rm keV}, \tag{15}$$

and for $B_\perp \sim 5$ μG and $E_e \sim 10$ TeV, this component should peak around $\sim$0.01 keV, with $B_\perp = B\sin\alpha'$ and α' the pitch angle. This is consistent with our findings in the next section.

3.2. Leptonic Modeling of the Broadband SED of Terzan 5

3.2.1. LESR and IC Components

We present new spectral fits[19] to the SED of Terzan 5 using the model of Kopp et al. (2013), as shown in Figure 1 (blue dashed lines). The model includes a spatial dimension, refined stellar soft-photon energy density profile, and full particle transport, taking diffusion and radiation losses into account with the assumptions of spherical symmetry and a steady-state regime.

In Figure 1, we indicate radio data (labeled "Effelsberg") associated with Region 11 (a prominent, large-scale, asymmetric feature offset from the center) as defined by Clapson et al. (2011). We fit these points with our predicted LESR component, in keeping with the suggestion by Clapson et al. (2011) that the flux from this region may be due to unpulsed SR from leptons that were injected by the MSPs into the GC and diffused throughout the cluster. Our predicted LESR component is much below the estimated BB flux level in the optical band (see Section 2.2). As mentioned in Equation (15), we expect this component to peak around 1 keV for particle energies $E_e \sim 100$ TeV and $B \sim 10$ μG. This led Kopp et al. (2013) to fit the X-ray surface brightness profile measured by *Chandra* in order to constrain the diffusion coefficient to $\kappa \sim 3.3 \times 10^{25}$ cm^2 s^{-1} at 1 TeV, similar to Equations (4) and (11). However, although their model prediction reproduced the flux level at a few keV, they could not fit the spectral slope of the observed data. This implies that the observed diffuse X-ray emission may be due to a different spectral component. We therefore now choose the maximum particle energy $E_{e,\rm max} = 10$ TeV and a slightly lower B-field of $B = 4$ μG so that our new LESR component peaks around $E_\gamma \sim 0.01$ keV (as we found in Section 3) and thus cuts off below the *Chandra* data. Furthermore, the low-energy tail of our predicted IC component satisfies the new *Fermi* data and upper limits, and we also reproduce the H.E.S.S. data.

3.2.2. Primary CR and Pair HESR Components

We use the model of Harding & Kalapotharakos (2015) to fit the GeV and keV data. Similar to previous studies (e.g., Harding et al. 2005; Venter et al. 2009; Zajczyk et al. 2013), we fit the *Fermi* LAT data using the cumulative primary CR component of pulsed γ-ray emission originating in the MSP magnetospheres (GeV component indicated by a solid red line and labeled "CR" in Figure 1). This has been a standard interpretation for the GeV spectrum measured by the LAT for several GCs (Abdo et al. 2010).

Following the idea of Kopp et al. (2013), we propose that the *Chandra* data indicate the presence of a "new" HE SR (HESR) component that has not been modeled in detail in this context[20] before: the cumulative pulsed SR from pairs generated within the magnetospheres of the host MSPs, radiating at altitudes that are a substantial fraction of the light cylinder (at a radius $R_{\rm LC} = c/\Omega$, with Ω the angular speed, where the corotational speed equals c) through cyclotron resonant absorption of radio photons (see Harding et al. 2008). Given the much higher local B-field (e.g., the magnetospheric field at the MSPs' light cylinder may reach $B_{\rm HESR} \sim 10^6$ G for the most energetic ones[21] versus the much lower GC field $B_{\rm LESR} \sim 10^{-5}$ G) and the much smaller average pitch angle ($\alpha_{\rm HESR} \sim 0.1$ versus $\alpha_{\rm LESR} \sim \pi/2$ rad), as well as different particle energies, the cutoff energy of this new component is much higher than that of the LESR spectrum:

$$\frac{E_{\rm HESR,cut}}{E_{\rm LESR,cut}} \sim \left(\frac{\gamma_{\rm SR}}{\gamma_{\rm LESR}}\right)^2 \frac{B_{\rm HESR}\sin\alpha_{\rm HESR}}{B_{\rm LESR}\sin\alpha_{\rm LESR}} \tag{16}$$

$$\sim \left(\frac{10^4}{10^7}\right)^2 \frac{10^6\ {\rm G} \times 10^{-1}}{10^{-5}\ {\rm G}} \sim 10^4. \tag{17}$$

This simple scaling predicts a cutoff $E_{\rm HESR,cut} \lesssim 100$ keV and thus provides us with a low-energy tail that might fit the X-ray data. This idea is also supported by observations of sources embedded in 47 Tucanae: Bogdanov et al. (2008) noted that even though most of the observed MSPs exhibit soft thermal spectra, three of them manifest hard power-law components. These components may plausibly be attributed to binary shock emission or magnetospheric SR. It is furthermore supported by detection of hard nonthermal X-ray emission from a number of field MSPs.

As a proof of principle, we now calculate model spectra invoking a cumulative pulsed HESR component originating in the MSP magnetospheres to fit the *Chandra* data (keV component indicated by a solid red line and labeled as "HESR" in Figure 1). We use a force-free B-field in the inertial observer frame, choosing a slot gap width of $0.03\Theta_{\rm PC}$, with

[19] The main aim of this paper is to ascertain whether we can elucidate the broadband spectral emission properties of Terzan 5, as well as those of the underlying sources that inject particles into Terzan 5. However, we realize that the energy-dependent morphology of this cluster is quite complex, so much so that it challenges the idea of a single (collective) particle population injected by the MSPs being responsible for all spectral emission components originating from partially overlapping spatial regions of different extents. Yet, to facilitate usable conclusions to be drawn from the current data, we do invoke a single population and study the source energetics, while deferring a study of the spatial properties of Terzan 5 to future work.

[20] As a practical measure, we attribute the *Chandra* data solely to collective, pulsed, nonthermal, magnetospheric pulsar emission. There could be contributions by other sources, but we do not know a priori the properties of unresolved stellar members hosted by Terzan 5.

[21] The average B-field at the light cylinder may be closer to $\sim 10^4$ G; however, the pair SR component is likely dominated by the MSPs with the highest spin-down luminosities and B-fields.

Θ_{PC} the polar-cap angle (the inner and outer angular boundaries of the gap were set at open-volume coordinates $r_{ovc} \in (0.90, 0.93)$, where the r_{ovc} coordinate labels self-similar rings, $r_{ovc} = 0$ being the magnetic pole and $r_{ovc} = 1$ being the polar-cap rim; see Dyks & Harding 2004), and a constant E-field from the MSP surface to $2R_{LC}$, set by an inverse acceleration length scale of $R_{acc} = d\gamma_e/dl = 2\,\mathrm{cm}^{-1}$ (i.e., $E_{||} = R_{acc} m_e c^2/e$, with γ_e the particle Lorentz factor and dl the step length along the particle trajectory, m_e and e the electron mass and charge). We divide the fraction of stellar surface covered by B-field line foot points that are within the gap using four self-similar rings and 72 azimuthal divisions. We choose an average pulsar period of $\langle P\rangle = 7.7$ ms, and, by fixing the average surface B-field to $\langle B_s\rangle = 5.8 \times 10^9$ G and moment of inertia $\langle I\rangle = 1.56 \times 10^{45}\,\mathrm{g\,cm^2}$, we obtain $\langle \dot{P}\rangle \sim 7 \times 10^{-19}\,\mathrm{s\,s^{-1}}$ and $\langle \dot{E}\rangle \sim 9.08 \times 10^{34}\,\mathrm{erg\,s^{-1}}$. The latter may represent significant contributions from more energetic MSPs. Nonetheless, we take these values as representative[22] of the pulsars in Terzan 5. We furthermore use a polar-cap pair spectrum calculated for an offset polar-cap B-field (Harding & Muslimov 2011a, 2011b; Barnard et al. 2016) with an offset parameter of $\epsilon = 0.6$. We choose an average magnetic inclination angle of $\langle\alpha\rangle = 45°$ and average observer angle of $\langle\zeta\rangle = 60°$ (for both HESR and CR components). See Harding & Kalapotharakos (2015) for details.

The number of visible γ-ray pulsars (N^{γ}_{vis}) is constrained by the primary CR flux level for a given set of model parameters. Alternatively, if we fix $N^{\gamma}_{vis} = N^{rad}_{vis} = 37$ to the number of visible radio pulsars (since nearly all currently detected γ-ray MSPs by *Fermi* are radio-loud), we may constrain other parameters, such as the gap width and average pulsar geometry α and ζ, or $\langle P\rangle$ and $\langle\dot{P}\rangle$. Unfortunately, it is difficult to break this degeneracy using X-ray data, since one may expect that $N^{X}_{vis} \lesssim N^{\gamma}_{vis}$ if their X-ray beams are slightly narrower than the γ-ray ones, and equality may not hold exactly. One may additionally write that $N^{X}_{tot} = N^{X}_{vis} + N^{X}_{invis} \geqslant N^{rad}_{vis} = 37$ and $N^{\gamma}_{vis} \geqslant 37$. The product $M_{\pm}N^{X}_{vis}$ is being set by the LESR flux level, so these two parameters are degenerate. Using the HESR (*Chandra*) flux level, we constrain the product $N^{X}_{vis}\langle M_{\pm}\rangle \sim 1.9 \times 10^4$, with $\langle M_{\pm}\rangle$ the average number of pairs produced per primary extracted from the polar cap per pulsar (the average electron–positron pair multiplicity). If we take $N^{X}_{vis} \approx 35$, we obtain $\langle M_{\pm}\rangle \approx 540$. However, this value crucially depends on the assumptions of the magnetospheric model: more optimistic assumptions about the electrodynamics (e.g., a higher B-field or current that will influence the particle transport) may lead to a larger single-MSP spectrum and yield a lower constant (value for the product of $N^{X}_{vis}\langle M_{\pm}\rangle$), thus lowering the value for $\langle M_{\pm}\rangle$.

Previously, Kopp et al. (2013) found an optimal source strength of $Q_0 \sim 6 \times 10^{33}\,\mathrm{erg^{-1}\,s^{-1}}$ when fitting the LESR and IC components. The value of Q_0 is usually constrained by assuming a parametric form for the particle injection spectrum

$$Q(E_e) = Q_0 E_e^{-\Gamma} \tag{18}$$

and using conservation of charge and energy per unit time (i.e., conservation of current and luminosity; Büsching et al. 2008; Venter et al. 2015c),

$$\int_{E_{e,min}}^{E_{e,max}} Q(E_e)\,dE_e = N_{MSP,tot}(\langle M_{\pm}\rangle + 1)\langle \dot{n}_{GJ}\rangle, \tag{19}$$

$$\int_{E_{e,min}}^{E_{e,max}} E_e Q(E_e)\,dE_e = N_{MSP,tot}\eta_p\langle\dot{E}\rangle, \tag{20}$$

with $\langle \dot{n}_{GJ}\rangle = 4\pi^2 B_s R^3/ceP^2 \propto \langle\dot{E}\rangle^{1/2}$ the average Goldreich–Julian rate of particles injected per second for a pulsar period P, surface magnetic field B_s, and stellar radius R (Goldreich & Julian 1969), and η_p the efficiency of converting the average spin-down luminosity to particle power. The "+1" in the first equation above represents the contribution from primary particles. The above system of equations may have up to 10 free parameters, implying a large degeneracy of parameters. We found an optimal value of $Q_0 \sim 1.4 \times 10^{34}\,\mathrm{erg^{-1}\,s^{-1}}$ (Figure 1) by fitting the unpulsed spectral components (for particular choices of other free parameters, e.g., κ and B, and using $\langle\dot{E}\rangle = 9.08 \times 10^{34}\,\mathrm{erg\,s^{-1}}$, $\eta_p = 3\%$, and $N_{MSP,tot} \sim 40$). This leads to a constraint on the average multiplicity,

$$\begin{aligned}\langle M_{\pm}\rangle &= \frac{Q_0(E_{e,max}^{1-\Gamma} - E_{e,min}^{1-\Gamma})}{(1-\Gamma)N_{MSP,tot}\langle\dot{n}_{GJ}\rangle} - 1 \\ &\approx 20\left(\frac{\eta_p}{3\%}\right)\left(\frac{2.7 \times 10^{32}\ \mathrm{s^{-1}}}{\langle\dot{n}_{GJ}\rangle}\right)\left(\frac{\langle\dot{E}\rangle}{9 \times 10^{34}\ \mathrm{erg\,s^{-1}}}\right) \\ &\propto \langle\dot{E}\rangle^{1/2},\end{aligned} \tag{21}$$

with the value of $\langle\dot{n}_{GJ}\rangle$ reflecting the choice for the average $\langle P\rangle$ and $\langle B_s\rangle$ of the MSPs, as mentioned earlier, for consistency. This estimate of $\langle M_{\pm}\rangle \approx 20$ is quite a bit lower than the previous one of $\langle M_{\pm}\rangle \approx 540$, as inferred from the HESR component. There are ways to mitigate this difference, given the uncertainty and degeneracy in several model parameters. The estimate of $\langle M_{\pm}\rangle$ using the unpulsed spectral components may be raised to $\langle M_{\pm}\rangle \approx 60$ by using $E_{min} \sim 40$ GeV, $E_{max} \sim 7$ TeV, and $\Gamma = 1.6$ without significantly changing the SED. Next, the discrepancy can be lowered to a factor of $\sim$4.5 by increasing $\langle I\rangle$ by a factor of $\sim$2, since $\langle M_{\pm}\rangle \propto \dot{E}^{1/2}$ for the unpulsed case, while $\langle M_{\pm}\rangle \propto \langle\dot{E}\rangle^{-1/2}$ for the pulsed case. This, however, raises $Q_0 \propto \langle\dot{E}\rangle$ by a factor of $\sim$2 so that LESR overshoots the data slightly, but this effect can then be mitigated by choosing $B \approx 1$ μG. The remaining discrepancy of a factor of $\sim$4.5 can be ameliorated by assuming a larger value for $\epsilon \sim 0.7$ (implying more pairs) and a larger gap width (say, increasing the upper boundary to $r_{ovc} \sim 0.96$, implying a larger active area on the stellar surface and thus lowering the demand on $\langle M_{\pm}\rangle$). There are also uncertainties in the angles $\langle\alpha\rangle$ and $\langle\zeta\rangle$ that may have a significant effect on the HESR flux. Lastly, using average values $\langle B_s\rangle$ and $\langle P\rangle$ leads to average values for $\langle\dot{n}_{GJ}\rangle$ and $\langle\dot{E}\rangle$, and this introduces further uncertainty. It is thus possible to pick (nonunique combinations of) values for some model parameters that would make the two estimates of $\langle M_{\pm}\rangle$ (using the pulsed and unpulsed SED components) consistent with each other without violating the observed SED.

[22] Unfortunately, there is a large uncertainty in the MSP population's properties. While a full Monte Carlo investigation of the SED may be preferable from a first-principles point of view, this will introduce many more uncertainties and a large range for the SED components' shapes and levels, so this will probably not lead to any conclusive answers. We therefore deem the approach of studying the behavior of an "average MSP" as the most practical, although we are cognizant of the fact that a particularly powerful MSP may skew the results.

The actual value of $M_{\pm}$ for MSPs is quite uncertain. Polar-cap pair cascades in a pure dipole field give very low values of $M_{\pm}$ for the bulk of MSPs, which prompted the suggestion that distortions of the *B*-field near the neutron star could increase $M_{\pm}$ (Harding & Muslimov 2011b), but the magnitude and structure of such distortions are not known. Comparing the results of particle-in-cell simulations (Kalapotharakos et al. 2018) with the γ-ray spectral cutoffs seen in *Fermi* pulsars can give the estimates of MSP $M_{\pm}$ needed to screen the global electric fields. This study indicates that the estimated MSP $M_{\pm}$ span a large range from 1 to 10^3.

3.2.3. Balancing the Energetics of the MSP Population

Our model provides reasonable fits to the *Chandra* and *Fermi* data for typical model parameters. However, one also has to consider whether this scenario is plausible in terms of energetics and the sensitivity of *Chandra*; i.e., would *Chandra* have seen these "unresolved MSPs" postulated by the model to explain the diffuse X-ray flux seen by Eger et al. (2010), or can one indeed explain the observed SR flux by a reasonable number of visible and invisible (unresolved) MSPs? The answer to this question lies in the (uncertain) population properties and emission energetics of the MSPs. We investigate this question by taking two approaches below.

From the *Chandra* data analysis, we can obtain three constraints. Eger et al. (2010) assumed a point-source sensitivity of $\sim 2\times10^{-15}\,\mathrm{erg\,s^{-1}\,cm^{-2}}$ in the 0.5–7.0 keV band. This leads to the first constraint of the minimum detectable luminosity of (i) $L_{\rm X,Chandra}\sim 7\times10^{30}\,\mathrm{erg\,s^{-1}}$ for their assumed distance of $d=5.5$ kpc. This is similar to the value of $L_{\rm X,Chandra}\sim(1\text{–}3)\times10^{31}\,\mathrm{erg\,s^{-1}}$ for an assumed distance of $d=8.7$ kpc found by Heinke et al. (2006). Let us adopt the first value. Second, Eger et al. (2010) noted that the total observed unabsorbed diffuse excess luminosity[23] is $L_{\rm X,tot}=2\times10^{33}\,\mathrm{erg\,s^{-1}}$ and estimated that the contribution of unresolved point sources[24] in the 1′–3′ region is $=7\times10^{31}\,\mathrm{erg\,s^{-1}}$. We thus set (ii) $L_{\rm X,vis}=2\times10^{33}$–$7\times10^{31}\,\mathrm{erg\,s^{-1}}=1.93\times10^{33}\,\mathrm{erg\,s^{-1}}$ and (iii) $L^{\rm X}_{\rm invis}=7\times10^{31}\,\mathrm{erg\,s^{-1}}$. In order to convert X-ray luminosities to pulsar spin-down values, one needs an efficiency factor $\eta_{\rm X}$:

$$L_{\rm X,vis}=\eta^{\rm X}_{\rm vis}N^{\rm X}_{\rm vis}\langle\dot{E}\rangle_{\rm vis}, \tag{22}$$

$$L_{\rm X,invis}=\eta^{\rm X}_{\rm invis}N^{\rm X}_{\rm invis}\langle\dot{E}\rangle_{\rm invis}, \tag{23}$$

with the total number of MSPs $N^{\rm X}_{\rm tot}=N^{\rm X}_{\rm vis}+N^{\rm X}_{\rm invis}\geqslant N^{\rm rad}_{\rm vis}=37$. This is a very unconstrained system of equations. To simplify this, one may assume that the whole population of MSPs may be characterized by a single $\eta_{\rm X}=\eta^{\rm X}_{\rm vis}=\eta^{\rm X}_{\rm invis}$. Division of the former equation by the latter and fixing $\langle\dot{E}\rangle_{\rm vis}$ then yields the following constraint:

$$N^{\rm X}_{\rm vis}\langle\dot{E}\rangle_{\rm vis}=k_{\rm L}N^{\rm X}_{\rm invis}\langle\dot{E}\rangle_{\rm invis}, \tag{24}$$

with $k_{\rm L}=L_{\rm X,vis}/L_{\rm X,invis}$ being a constant. While there is some degeneracy, this constraint may, e.g., be satisfied for the following choices: $\langle\dot{E}\rangle_{\rm vis}=9.08\times10^{34}\,\mathrm{erg\,s^{-1}}$, $\langle\dot{E}\rangle_{\rm invis}=8\times10^{33}\,\mathrm{erg\,s^{-1}}$, $N^{\rm X}_{\rm vis}=41$, and $N^{\rm X}_{\rm invis}=17$ (implying $\eta_{\rm X}=0.05\%$). If we adopt $\langle\dot{E}\rangle_{\rm vis}=1.8\times10^{34}\,\mathrm{erg\,s^{-1}}$ (e.g., Abdo et al. 2010), the following values satisfy the constraint above: $\langle\dot{E}\rangle_{\rm invis}=10^{33}\,\mathrm{erg\,s^{-1}}$, $N^{\rm X}_{\rm vis}=23$, and $N^{\rm X}_{\rm invis}=15$ (implying $\eta_{\rm X}=0.5\%$); alternatively, we can set $\langle\dot{E}\rangle_{\rm vis}=10^{34}\,\mathrm{erg\,s^{-1}}$, obtaining $\langle\dot{E}\rangle_{\rm invis}=2.8\times10^{32}\,\mathrm{erg\,s^{-1}}$, $N^{\rm X}_{\rm vis}=19$, and $N^{\rm X}_{\rm invis}=25$ (implying $\eta_{\rm X}=1\%$). These numbers seem reasonable and adhere to the constraint that $N^{\rm X}_{\rm tot}=N^{\rm X}_{\rm vis}+N^{\rm X}_{\rm invis}\geqslant N^{\rm rad}_{\rm vis}=37$. Thus, we consider our assumption of attributing the X-ray emission to the cumulative pair SR, as used in the previous section, plausible.

In an attempt to perform a more robust analysis, potentially obtain stronger constraints on the MSP population, and break some parameter degeneracies, we consider a parameterized pulsar spin-down luminosity function $N_{\rm MSP}(>\dot{E})\propto\dot{E}^{-\gamma_{\rm L}}$ (Johnston & Verbunt 1996). We will use this to balance the required X-ray energetics by assuming that $\dot{E}_{\rm vis}\propto L_{\rm X,vis}$ and $\dot{E}_{\rm invis}\propto L_{\rm X,invis}$. This implies $dN/d\dot{E}=N_0'(\dot{E}/\dot{E}_0)^{-(\gamma_{\rm L}+1)}$, with N_0' a normalization constant. Johnston & Verbunt (1996) inferred a typical GC value of $\gamma_{\rm L}\sim0.5$, while Heinke et al. (2006) found $\gamma_{\rm L}\sim0.4$–0.7 for Terzan 5, depending on the energy band. By defining $\dot{E}_{\rm b}=L_{\rm X,Chandra}/\eta_{\rm X}$, one can next recover the following quantities:

$$N^{\rm X}_{\rm tot}=\int_{\dot{E}_{\rm min}}^{\dot{E}_{\rm max}}\left(\frac{dN}{d\dot{E}}\right)d\dot{E}, \tag{25}$$

$$N^{\rm X}_{\rm vis}=\int_{\dot{E}_{\rm b}}^{\dot{E}_{\rm max}}\left(\frac{dN}{d\dot{E}}\right)d\dot{E}, \tag{26}$$

$$N^{\rm X}_{\rm invis}=\int_{\dot{E}_{\rm min}}^{\dot{E}_{\rm b}}\left(\frac{dN}{d\dot{E}}\right)d\dot{E}, \tag{27}$$

$$\langle\dot{E}\rangle_{\rm vis}=\frac{1}{N^{\rm X}_{\rm vis}}\int_{\dot{E}_{\rm b}}^{\dot{E}_{\rm max}}\dot{E}\left(\frac{dN}{d\dot{E}}\right)d\dot{E}, \tag{28}$$

$$\langle\dot{E}\rangle_{\rm invis}=\frac{1}{N^{\rm X}_{\rm invis}}\int_{\dot{E}_{\rm min}}^{\dot{E}_{\rm b}}\dot{E}\left(\frac{dN}{d\dot{E}}\right)d\dot{E}. \tag{29}$$

We want to solve for four quantities: $\dot{E}_{\rm min}$, $\dot{E}_{\rm max}$, N_0' (or, equivalently, $N^{\rm X}_{\rm tot}$), and $\gamma_{\rm L}$; once these are fixed, we can infer the MSP population properties through the above equations. We note, however, that we are using this luminosity function to fit X-ray luminosities, which are integral quantities. We therefore expect to find degenerate solutions, as different combinations might yield the same integral luminosities. Thus, we need four constraints or measurements. We can use the same three constraints as before. Crucially, one needs to specify a fourth parameter $\eta_{\rm X}$ to convert from spin-down luminosities to X-ray luminosities. By fixing $\eta_{\rm X}$, we implicitly fix the product $N^{\rm X}_{\rm vis}\langle\dot{E}\rangle_{\rm vis}$. As a first attempt, let us assume

[23] We note that the power-law fit to the data implies that the visible nonthermal luminosity is $L_{\rm X,vis}=8.52\times10^{32}\,\mathrm{erg\,s^{-1}}$ (Eger et al. 2010), using data from annuli lying between 55″ and 174″. By integrating our predicted $E\text{-}dN/dE\gamma$ HESR spectrum in the 1–7 keV band, we find $L_{\rm X,HESR}\sim5.5\times10^{32}\,\mathrm{erg\,s^{-1}}$. This is close to this luminosity, with the discrepancy explained by the fact that the model does not perfectly match the data in terms of the spectral slope. However, this power-law luminosity is a factor of ∼2 lower than the total observed luminosity as noted in the main text, which is also the number quoted by Eger et al. (2010) in their interpretation section. We decided to use the higher value, following this usage by Eger et al. (2010), and note that if we use the lower value, the solutions in Table 2 have similar best-fit parameters but with lower MSP numbers reflecting the lower value of $L_{\rm X,vis}$ in this case.

[24] We use the label "invisible" in what follows to refer to those pulsars that have too low a spin-down luminosity to be detectable as single point sources by *Chandra* but that may contribute to the cumulative unresolved point-source luminosity as a population of low-energetic pulsars. As before, we discard the contribution of other source classes to this unresolved luminosity.

Table 2
Sample Parameter Combinations that Lead to a Balance of the X-Ray-implied Energetics

η_X	$\langle\dot{E}\rangle_{invis}$	$\langle\dot{E}\rangle_{vis}$	$\dot{E}_{min}$	$\dot{E}_{max}$	γ_L	N^X_{vis}	N^X_{invis}	N^X_{tot}
0.05%	3.0×10^{33}	9.2×10^{34}	10^{31}	2.4×10^{35}	−0.19	43	45	88
0.05%	3.5×10^{32}	1.8×10^{35}	10^{29}	10^{36}	0.21	22	399	421
0.5%	1.2×10^{32}	3.8×10^{34}	10^{31}	10^{36}	0.50	10	116	126
0.5%	1.5×10^{32}	2.9×10^{34}	10^{31}	3.6×10^{35}	0.40	14	96	110
1%	7.4×10^{31}	2.5×10^{34}	10^{31}	2.0×10^{36}	0.60	8	95	103
1%	1.3×10^{32}	2.4×10^{34}	3.0×10^{31}	2.9×10^{36}	0.64	8	53	61
1%	2.5×10^{32}	2.0×10^{34}	10^{32}	3.0×10^{36}	0.69	10	27	37

Note. The units of the spin-down luminosities are erg s^{-1}.

$\eta_X = 0.05\%$ (e.g., for $N^X_{vis} = 41$ and $\langle\dot{E}\rangle_{vis} = 9.08 \times 10^{34}$ erg s^{-1} to make the calculation consistent with the previous estimate). It is difficult to obtain the actual value for $\langle\dot{E}\rangle_{vis}$, given the effect of the GC cluster potential on the $\dot{P}$ of each MSP (e.g., Bogdanov et al. 2008). If we could, this would further constrain the system via Equation (28). Heinke et al. (2006) noted that while they did not detect an X-ray MSP explicitly, one X-ray source could plausibly be an MSP based on the proximity to a radio MSP position; they also noted that more identifications of X-ray MSPs could be made as radio positions become available. We thus have additional constraints $N^X_{vis} \gtrsim 1$ and $N^X_{tot} \geqslant N^{rad}_{vis}$ (which may be used as checks on the consistency of the solutions we obtain). We do obtain a nonunique solution for each fixed value of η_X. However, η_X is not known, and the parameters that satisfy the other three constraints are quite degenerate, as expected. Table 2 indicates a number of parameter combinations that satisfy the observational constraints.[25] It is clear that a different choice of η_X will favor a different solution that will imply a different value of $\langle\dot{E}\rangle_{vis}$ (which also depends on the average moment of inertia $\langle I\rangle$, $\langle P\rangle$, and $\langle\dot{P}\rangle$). For example, a higher value of η_X will yield a lower value of $\langle\dot{E}\rangle_{vis}$ or $\langle I\rangle$ for a given value of N^X_{vis} and keeping other parameters fixed. If we require $\langle\dot{E}\rangle_{vis}$ to be the same as assumed in the model used to predict the pulsed emission, this may lead to unrealistic values for γ_L for a given η_X. Relaxing this requirement (which may easily be done, given other parameter uncertainties) implies more suitable values for the other parameters. It is therefore clear that the system of equations is very coupled and the parameters are degenerate, given the lack of suitable constraints. One may think to constrain the solution space by requiring $N^X_{tot} = N^\gamma_{tot} \approx N^\gamma_{vis} = 180^{+120}_{-100}$, the latter being the estimated total number of visible MSPs in Terzan 5 as inferred from the *Fermi*-measured GeV energy flux (Abdo et al. 2010). However, this estimate is quite uncertain and does not contain uncertainties in distance (the square of which determines the γ-ray luminosity L_γ) and conversion efficiency of $\dot{E}_{vis}$ to L_γ, so this does not seem to be a strong constraint. Likewise, we chose $N^\gamma_{tot} = 37$ when fitting the CR component, but this value is also subject to other model assumptions, such as MSP geometry and gap width. Finally, it seems that the last few entries in Table 2 might be the more plausible combinations in view of the independent constraints on $\gamma_L \sim 0.4$–0.7 and $N^X_{vis} \gtrsim 1$ (i.e., probably relatively small numbers of visible X-ray pulsars) gleaned from the analysis of Heinke et al. (2006). Thus, the uncertainty in several parameters, particularly η_X, as well as parameter degeneracies preclude us from making definite statements about the MSP population properties. Yet we see that there are several plausible solutions that characterize and constrain the MSP population's energetics, implying that the scenario of MSPs being responsible for the broadband SED may be justified and thus plausible.

Gonthier et al. (2018) derived a luminosity function for MSPs in 47 Tucanae through a population synthesis that fits the *Fermi* spectrum, presumed to be the combined emission from all MSPs in the cluster. They found a γ-ray luminosity distribution that peaks at $\sim 10^{33}$ erg s^{-1} and a spin-down power distribution peaking at $\sim 2 \times 10^{34}$ erg s^{-1}, extending down to $\sim 10^{30}$ erg s^{-1}, with a γ-ray efficiency around 0.1. Their peak $\dot{E}$ value is similar to the $\langle\dot{E}_{vis}\rangle$ we have derived for Terzan 5.

The bulk of visible radio MSPs occur in the core of the cluster, and one expects the majority of pulsars here to be due to the deep potential well of the GC. However, one may expect to find a small number of MSPs farther out, depending on their birth and evolutionary history. The fact that the diffuse X-ray flux profile measured by Eger et al. (2010) drops off slightly slower than the generalized King profile fit (e.g., King 1962) to the detected X-ray point-source distribution (Heinke et al. 2006), as well as the infrared surface brightness profile measured by Trager et al. (1995), may support this idea, and a (slowly) decreasing MSP density with radius may plausibly correlate with the observed decreasing X-ray flux profile. Eger et al. (2010) detected nonthermal X-ray emission beyond the half-mass radius of Terzan 5. If we take the above energetics argument as plausible, this would imply possibly tens of unresolved MSPs and a handful MSPs that are, in principle, visible in X-rays in this region. This would also imply that even more MSPs should be visible in X-rays at the core versus outer reaches of the GC, but we do not have constraints on the diffuse X-ray emission at the GC center at this stage, and source confusion in this dense region may complicate the matter. Future constraints on the central diffuse X-ray emission, spatial distribution of the MSP population, and average expected multiplicity and spin-down power will thus more deeply probe our hypothesis that the HESR component is due to magnetospheric, pulsed SR from pairs.

[25] A preliminary Markov chain Monte Carlo investigation (Foreman-Mackey et al. 2013) confirmed the degenerate nature of the free parameters (some are correlated), as well as their being quite unconstrained (reflected by asymmetrical and flat probability distributions, as well as elongated confidence contours). Best-fit values furthermore depend on the choice of priors/parameter bounds. The median values are, however, similar to those in Table 2.

4. Conclusions

The main focus of this paper has been twofold: to gather more data on Terzan 5 and to scrutinize ideas about the particle sources and emission processes responsible for the broadband emission spectrum we observe from this cluster. Our models postulated four spectral components (LESR, HESR, CR, and IC) and attempted to constrain the MSP population's distribution of spin-down luminosity using the observed X-ray diffuse emission.

We obtained new *Fermi* data that we could fit using a model for the cumulative CR from a population of MSPs embedded within Terzan 5. These data also proved to be constraining for the low-energy tail of the unpulsed IC component, yielding a particle efficiency of $\eta_{\rm p} \sim 3\%$, depending on the choice of several parameters, notably $\langle \dot{E}_{\rm vis} \rangle$ and $N_{\rm MSP,tot}$.

We demonstrated that we could fit the radio spectral points by invoking an LESR component that might extend into the optical range. We furthermore argued that our predicted LESR flux is far below the expected thermal optical flux level. Thus, obtaining an upper limit on the nonthermal flux in the optical band would be very difficult, given the roughly $N_* \sim 10^{5-6}$ point sources that have to be subtracted from an optical map of the GC. Even when performing and subtracting a King model fit to the surface brightness profile, the uncertainty on the remaining diffuse flux would be very large. However, since the BB spectrum occurs over a much narrower energy range than the LESR, there may yet be hope of detecting the latter outside of the optical range.

Bednarek et al. (2016) concurred with our prior predictions (Venter & de Jager 2008; Venter et al. 2009; Kopp et al. 2013) that GCs should typically have SR components that peak in the optical/ultraviolet range but also pointed out the problem of the dominating radiation field produced by the large population of GC stars. They furthermore mentioned that quite atypical parameters (a combination of very large cluster *B*-fields and particle energies) would be needed in order to produce an observable level of X-ray flux. Lastly, it would be problematic to compare optical and X-ray brightness profiles, since the underlying source distributions have different spatial and emission characteristics. The respective telescope point-spread functions also differ, compounding the problem. Also, the observed *Chandra* spectrum is not well fit by a single LESR component. To solve these problems and still fit the observed data, we invoked a new component to explain the hard *Chandra* spectrum: cumulative SR from pair plasma in MSP magnetospheres. The low-energy tail of this HESR component reproduces the spectral slope of the X-ray data quite well. We argued that the required energetics and numbers of the MSP source population needed to reproduce the detected diffuse X-ray emission are plausible, albeit not very well constrained (although X-ray efficiencies of $\eta_{\rm X} \sim 1\%$ and thus $\gamma_{\rm L} \sim 0.7$ and $N_{\rm vis}^{\rm X} \sim 10$ may be preferable). The MSP scenario to explain the broadband SED of Terzan 5 should thus be further scrutinized by future constraints on the properties (e.g., number of visible X-ray pulsars and their average spin-down luminosity) of the MSPs embedded in this GC.

For the VHE band, there were no new data available. The HE tail of our predicted unpulsed IC component produced a good fit to the current H.E.S.S. data. More data obtained by H.E.S.S. or new data from the CTA may better constrain the shape and cutoffs of the IC component owing to the lower energy threshold, as well as increased sensitivity of the latter. This may limit the particle minimum and maximum energies, source strength, and average multiplicity, as well as the conversion efficiency of spin-down luminosity to particle power.

We have modeled the pulsed SR and CR components using a magnetospheric pulsar model, while we have modeled the LESR and IC components using an independent transport and emission model. While we have attempted to apply both these codes simultaneously for consistent parameter choices, a unified approach may lead to even deeper constraints on the cluster environment and stellar members.

The morphology of structures associated with Terzan 5 differs significantly in extent and position for the different energy bands, challenging the idea that a single particle population is responsible for all spectral components. Higher-resolution images of the GC will aid in elucidating the spatial properties of the different emission structures, possibly constraining the diffusion coefficient and cluster *B*-field profile.

Using Terzan 5 as a case study, we could constrain our leptonic model for broadband emission from GCs. The CTA will probably detect many more VHE GCs (Ndiyavala et al. 2018), while multiwavelength data on these sources should also continue to improve in both quantity and quality. This will allow us to further scrutinize competing emission models, as well as developing new, more complete and comprehensive ones that might explain the spatial and spectral properties of Galactic GCs at an ever-increasing level of detail.

We acknowledge fruitful discussions with Michael Backes, Carlo van Rensburg, Matthew Kerr, Hongjun An, Daniel Castro, Gudlaugur Johannesson, and Philippe Bruel. This work is based on research supported wholly/in part by the National Research Foundation of South Africa (NRF; grant Nos. 81671, 87613, 90822, 92860, 93278, and 99072). The grant holder acknowledges that opinions, findings, and conclusions or recommendations expressed in any publication generated by the NRF-supported research is that of the author(s), and that the NRF accepts no liability whatsoever in this regard. A.K.H. acknowledges support from the NASA Astrophysics Theory Program. C.V. and A.K.H. acknowledge support from the *Fermi* Guest Investigator Program.

The *Fermi* LAT Collaboration acknowledges generous ongoing support from a number of agencies and institutes that have supported both the development and the operation of the LAT, as well as scientific data analysis. These include the National Aeronautics and Space Administration and the Department of Energy in the United States; the Commissariat à l'Energie Atomique and the Centre National de la Recherche Scientifique/Institut National de Physique Nucléaire et de Physique des Particules in France; the Agenzia Spaziale Italiana and the Istituto Nazionale di Fisica Nucleare in Italy; the Ministry of Education, Culture, Sports, Science and Technology (MEXT), High Energy Accelerator Research Organization (KEK), and Japan Aerospace Exploration Agency (JAXA) in Japan; and the K. A. Wallenberg Foundation, the Swedish Research Council, and the Swedish National Space Board in Sweden.

Additional support for science analysis during the operations phase is gratefully acknowledged from the Istituto Nazionale di Astrofisica in Italy and the Centre National d'Études Spatiales

in France. This work was performed in part under DOE contract DE-AC02-76SF00515.

Facilities: *Fermi* Large Area Telescope, Effelsberg Radio Telescope, *Chandra* X-ray Satellite, H.E.S.S.

ORCID iDs

H. Ndiyavala https://orcid.org/0000-0001-9279-1775
C. Venter https://orcid.org/0000-0002-2666-4812
A. K. Harding https://orcid.org/0000-0001-6119-859X
D. A. Smith https://orcid.org/0000-0002-7833-0275
A. Kopp https://orcid.org/0000-0001-5206-9606
D. J. van der Walt https://orcid.org/0000-0001-6666-6866

References

Abdo, A. A., Ackermann, M., Ajello, M., et al. 2009, Sci, 325, 845
Abdo, A. A., Ackermann, M., Ajello, M., et al. 2010, A&A, 524, A75
Abdo, A. A., Ajello, M., Allafort, A., et al. 2013, ApJS, 208, 17
Abramowski, A., Acero, F., Aharonian, F., et al. 2011a, ApJ, 735, 12
Abramowski, A., Acero, F., Aharonian, F., et al. 2011b, A&A, 531, L18
Abramowski, A., Acero, F., Aharonian, F., et al. 2013, A&A, 551, A26
Acero, F., Ackermann, M., Ajello, M., et al. 2015, ApJS, 218, 23
Acero, F., Ackermann, M., Ajello, M., et al. 2016, ApJS, 223, 26
Aharonian, F., Akhperjanian, A. G., Anton, G., et al. 2009, A&A, 499, 273
Anderhub, H., Antonelli, L. A., Antoranz, P., et al. 2009, ApJ, 702, 266
Atoyan, A., Buckley, J., & Krawczynski, H. 2006, ApJL, 642, L153
Atwood, W. B., Abdo, A. A., Ackermann, M., et al. 2009, ApJ, 697, 1071
Atwood, W. B., Albert, A., Baldini, L., et al. 2013, arXiv:1303.3514
Barnard, M., Venter, C., & Harding, A. K. 2016, ApJ, 832, 107
Bednarek, W. 2011, in High-energy Emission from Pulsars and their Systems, ed. D. F. Torres & N. Rea (Berlin: Springer), 185
Bednarek, W. 2012, JPhG, 39, 065001
Bednarek, W., & Sitarek, J. 2007, MNRAS, 377, 920
Bednarek, W., Sitarek, J., & Sobczak, T. 2016, MNRAS, 458, 1083
Bednarek, W., & Sobczak, T. 2014, MNRAS, 445, 2842
Bhatia, V. B., Mishra, S., & Panchapakesan, N. 1992, JApA, 13, 287
Bogdanov, S., Grindlay, J. E., & Rybicki, G. B. 2008, ApJ, 689, 407
Brown, A. M., Lacroix, T., Lloyd, S., Bœhm, C., & Chadwick, P. 2018, PhRvD, 98, 041301
Büsching, I., de Jager, O. C., Potgieter, M. S., & Venter, C. 2008, ApJL, 678, L39
Cadelano, M., Ransom, S. M., Freire, P. C. C., et al. 2018, ApJ, 855, 125
Camilo, F., & Rasio, F. A. 2005, ASPC, 328, 147
Chen, K. 1991, Natur, 352, 695
Cheng, K. S., Chernyshov, D. O., Dogiel, V. A., Hui, C. Y., & Kong, A. K. H. 2011, ApJ, 723, 1219
Clapson, A.-C., Domainko, W., Jamrozy, M., Dyrda, M., & Eger, P. 2011, A&A, 532, 47
Cohn, H. N., Lugger, P. M., Grindlay, J. E., & Edmonds, P. D. 2002, ApJ, 571, 818
Condon, J. J., Cotton, W. D., Greisen, E. W., et al. 1998, AJ, 115, 1693
de Jager, O. C., & Büsching, I. 2010, A&A, 517, L9
de Jager, O. C., Raubenheimer, B. C., & Swanepoel, J. W. H. 1989, A&A, 221, 180
de Menezes, R., Cafardo, F., & Nemmen, R. 2019, MNRAS, 486, 851
Domainko, W. F. 2011, A&A, 533, L5
Dyks, J., & Harding, A. K. 2004, ApJ, 614, 869
Eger, P., & Domainko, W. 2012, A&A, 540, A17
Eger, P., Domainko, W., & Clapson, A.-C. 2010, A&A, 513, A66
Ferraro, F. R., Dalessandro, E., Mucciarelli, A., et al. 2009, Natur, 462, 483
Foreman-Mackey, D., Hogg, D. W., Lang, D., & Goodman, J. 2013, PASP, 125, 306
Freire, P. C. C., Ridolfi, A., Kramer, M., et al. 2017, MNRAS, 471, 857
Fruchter, A. S., & Goss, W. M. 2000, ApJ, 536, 865
Goldreich, P., & Julian, W. H. 1969, ApJ, 157, 869
Gonthier, P. L., Harding, A. K., Ferrara, E. C., et al. 2018, ApJ, 863, 199
Harding, A. K., & Kalapotharakos, C. 2015, ApJ, 811, 63
Harding, A. K., & Muslimov, A. G. 2011a, ApJL, 726, L10
Harding, A. K., & Muslimov, A. G. 2011b, ApJ, 743, 181
Harding, A. K., Stern, J. V., Dyks, J., & Frackowiak, M. 2008, ApJ, 680, 1378
Harding, A. K., Tademaru, E., & Esposito, L. W. 1978, ApJ, 225, 226
Harding, A. K., Usov, V. V., & Muslimov, A. G. 2005, ApJ, 622, 531
Heinke, C. O., Wijnands, R., Cohn, H. N., et al. 2006, ApJ, 651, 1098
Hessels, J. W. T., Ransom, S. M., Stairs, I. H., et al. 2006, Sci, 311, 1901
Ivanova, N., Heinke, C. O., & Rasio, F. A. 2008, in AIP Conf. Ser. 983, 40 Years of Pulsars: Millisecond Pulsars, Magnetars and More, ed. C. Bassa et al. (Melville, NY: AIP), 442
Johnson, T. J., Ray, P. S., Roy, J., et al. 2015, ApJ, 806, 91
Johnston, H. M., & Verbunt, F. 1996, A&A, 312, 80
Kalapotharakos, C., Brambilla, G., Timokhin, A., Harding, A. K., & Kazanas, D. 2018, ApJ, 857, 44
Kerr, M. 2011, ApJ, 732, 38
King, I. R. 1962, AJ, 67, 471
Kong, A. K. H., Hui, C. Y., & Cheng, K. S. 2010, ApJ, 712, 36
Kopp, A., Venter, C., Büsching, I., & de Jager, O. C. 2013, ApJ, 779, 126
Lang, K. R. 1992, Astrophysical Data I. Planets and Stars (Berlin: Springer)
Lanzoni, B., Ferraro, F. R., Dalessandro, E., et al. 2010, ApJ, 717, 653
Lyne, A. G., Johnston, S., Manchester, R. N., Staveley-Smith, L., & D'Amico, N. 1990, Natur, 347, 650
Lyne, A. G., Mankelow, S. H., Bell, J. F., & Manchester, R. N. 2000, MNRAS, 316, 491
McCutcheon, M. 2009, arXiv:0907.4974
Ndiyavala, H., Krüger, P. P., & Venter, C. 2018, MNRAS, 473, 897
Nolan, P. L., Abdo, A. A., Ackermann, M., et al. 2012, ApJS, 199, 31
Prinsloo, P., Venter, C., Büsching, I., & Kopp, A. 2013, arXiv:1311.3791
Ransom, S. M., Hessels, J. W. T., Stairs, I. H., et al. 2005, Sci, 307, 892
Schlickeiser, R., & Ruppel, J. 2010, NJPh, 12, 3
Tam, P.-H. T., Hui, C. Y., & Kong, A. K. H. 2016, J. Astron. SS., 33, 1
The *Fermi* LAT Collaboration 2019, arXiv:1902.10045
Trager, S. C., King, I. R., & Djorgovski, S. 1995, AJ, 109, 218
Valenti, E., Ferraro, F. R., & Origlia, L. 2007, ApJ, 133, 1287
Venter, C., & de Jager, O. C. 2008, in AIP Conf. Ser. 1085, High Energy Gamma-Ray Astronomy (Melville, NY: AIP), 277
Venter, C., de Jager, O. C., & Clapson, A.-C. 2009, ApJL, 696, L52
Venter, C., & Kopp, A. 2015a, in Proc. SAIP2014, ed. C. Engelbrecht & S. Karataglidis (Pretoria: SAIP), 394
Venter, C., & Kopp, A. 2015b, MmSAI, 86, 70
Venter, C., Kopp, A., Harding, A. K., Gonthier, P. L., & Büsching, I. 2015c, ApJ, 807, 130
Verbunt, F., & Hut, P. 1987, in IAU Symp. 125, The Origin and Evolution of Neutron Stars, ed. D. J. Helfand & H. H. Huang (Dordrecht: Reidel), 187
Wei, D. M., Cheng, K. S., & Lu, T. 1996, ApJ, 468, 207
Wu, E. M. H., Hui, C. Y., Kong, A. K. H., et al. 2014, ApJL, 788, L40
Zajczyk, A., Bednarek, W., & Rudak, B. 2013, MNRAS, 432, 3462
Zhang, P. F., Xin, Y. L., Fu, L., et al. 2016, MNRAS, 459, 99